

Landslides (2019) 16:253–263
 DOI 10.1007/s10346-018-1088-8
 Received: 9 June 2018
 Accepted: 10 October 2018
 Published online: 24 October 2018
 © Springer-Verlag GmbH Germany
 part of Springer Nature 2018

José J. Lizárraga · Giuseppe Buscarnera

Spatially distributed modeling of rainfall-induced landslides in shallow layered slopes

Abstract The zoning of landslide susceptibility on layered landscapes is a key challenge for regional hazard analyses. From a modeling standpoint, the combination of transient infiltration and vertical heterogeneity can lead to hydro-mechanical processes that are difficult to incorporate in spatially distributed frameworks. In this work, a physically based model for the efficient generation of regional landslide susceptibility maps in layered landscapes is presented. The formulation involves the discretization of a digital terrain into slope units, thus enabling the incorporation of georeferenced datasets to define the input variables. Model computations rely on a vectorized finite element (FE) solver that performs simulations of vertical unsaturated flow and slope stability analyses. The framework allows the use of different meshes across the region to efficiently allocate the computational cost associated with layers of variable thickness and/or complex stratigraphy. The model is used to analyze a series of documented shallow landslides that occurred in a region covered by stratified volcanic deposits. In addition to the simulation of layered profiles constrained by field and laboratory data, two simplified scenarios are considered in which homogeneous slopes with different values of hydraulic conductivity K_s are used. It is shown that, while the homogeneous models may have an acceptable spatial performance in some sectors of the landscape, the use of homogenized values of K_s leads to inconsistent temporal sequences of landslide triggering, as well as to failure depths always located at the base of the slope. By contrast, the use of stratified profiles leads to an improved spatiotemporal performance over the whole region, as well as to computed failure depths that are consistent with landslide inventories. The proposed methodology provides a useful tool for landslide hazard studies in that it not only addresses the computational challenges associated with multiple slope stability analyses, but it also enables the incorporation of system properties that are often neglected in spatially distributed modeling frameworks.

Keywords Shallow landslides · Spatially distributed modeling · Infiltration · Heterogeneity · Unsaturated soils

Introduction

Regional zonation of landslide susceptibility is an important tool for risk assessment studies. Its development requires the analysis of multiple datasets to define zones of potential instability across a landscape and often requires the collection of detailed spatial information over the affected areas (Van Westen et al. 2008; Fressard et al. 2014). This is a challenging task for rainfall-induced shallow landsliding, in which numerous slope failures can occur within a temporal interval of few hours and involve areas of several km² (Baum et al. 2005; Crozier 2005; Van Westen et al. 2006). Such features often preclude an immediate use of site-specific slope stability analyses for landslide forecasting, thus motivating the use of alternative methodologies.

The advent of Geographical Information Systems (GIS) and the increasing availability of computational resources have led to the

development of spatially distributed models for landslide susceptibility (Godt et al. 2008). For physically based models, a standard computational approach consists of discretizing a landscape into slope units for which stability analyses are performed. In this manner, information from spatial datasets, such as Digital Elevation Models (DEM), remote sensing, and georeferenced surveys are used to define model conditions for each slope (Chen and Zhang 2014). A key component of such frameworks is the simulation of subsurface hydrologic processes. Earlier propositions were based on steady-state groundwater conditions, topographic indexes, and saturated soil properties to define critical thresholds for slope instability, which were eventually mapped across the landscape (Montgomery and Dietrich 1994). Subsequent formulations (Iverson 2000) simulated infiltration in quasi-saturated soils as a pore pressure diffusion process, thus enabling the incorporation of time-dependent rainfall input. More recently, an analytical solution for the Richards' equation has been used to simulate the transient infiltration process, thus allowing the incorporation of unsaturated soil properties (i.e., water retention models, hydraulic conductivity functions, effective stress) into stability analyses (Baum et al. 2010). While such formulations have proved useful in several geological contexts, they rely on the assumption of homogeneous slope, thus precluding its use in regions characterized by highly stratified soils.

In this work, a spatially distributed model for landslide susceptibility in stratified, unsaturated slopes is presented. The framework relies on a vectorized Finite Element (FE) algorithm that simultaneously solves the Richards' equation at multiple cells by sharing the same discretization parameters (i.e., mesh size and time steps). For this purpose, a description of the implementation procedures is first presented. Afterwards, the model is used to back-analyze a series of documented shallow landslides that occurred in a highly stratified volcanic setting, for which detailed laboratory and field datasets are used to constrain the model inputs (Bilotta et al. 2005; Crosta and Dal Negro 2003; Sorbino and Nicotera 2013). These results are finally compared against simulations relying on homogeneous slope profiles by analyzing the spatiotemporal performance of the different models and the computed failure depths.

Model description

Hydrological and mechanical modeling

For a given unsaturated slope, transient infiltration can be modeled by enforcing the water mass balance (Richards 1931):

$$nC_w(h) \frac{\partial h}{\partial t} = \nabla \cdot [K(h) \nabla (h + z)] \quad (1)$$

where n is the porosity, h is the pressure head induced by capillarity, t is time, z is the vertical coordinate, $K(h)$ is a hydraulic conductivity function (HCF), and $C_w(h)$ is the unsaturated storage coefficient (i.e., the rate of change of degree of saturation $S_r(h)$ with respect to h). The above equation supplemented with

constitutive relations, initial and boundary conditions constitute the initial boundary-value problem to solve for each slope unit within the landscape. Although surface runoff can be incorporated through enhanced boundary conditions and rerouting techniques (Camporese et al. 2010), this aspect was not tackled here for the sake of simplicity. In order to solve the equations numerically, the problem must be discretized in space and time and converted in algebraic form (Celia et al. 1990; Van Dam and Feddes 2000). For this purpose, here a Galerkin spatial discretization and an explicit forward temporal scheme have been used, respectively, by following standard computational techniques for multi-phase flow (Chen et al. 2006; Zienkiewicz et al. 1999).

Stability analyses require the definition of a factor of safety (FS). Although several forms of FS have been proposed in the literature (Duncan et al. 2014; Lu and Godt 2008), here the following expression previously calibrated for the soils of the study area will be used (Lizárraga and Buscarnera, 2017):

$$FS = \frac{\tan\phi'}{\tan\alpha} \left(1 + \frac{ks}{\sigma^{net}} \right) \quad (2)$$

where ϕ' and α are the friction angle of the layer and its slope inclination, respectively, σ^{net} is the net stress (in this case the overburden stress), and k is a parameter that quantifies the effect of suction s , on the shearing resistance (Fredlund et al. 1978).

Implementation

The model implementation is divided into three stages: *input*, *processing*, and *output*. The first stage involves the input of spatially distributed data and the definition of the model parameters. To facilitate data manipulation/visualization, each dataset is treated as a georeferenced grid within a GIS. The study area is discretized into m slope units (i.e., squared cells), as is schematically shown in Fig. 1, where $m = 9$. In addition to physical variables, the spatial distribution of FE discretization parameters (i.e., mesh and time steps) must be defined. This avoids the unnecessary use of the same mesh for all the slopes within the landscape, thus providing flexibility to efficiently distribute the computational cost associated with thicker layers and/or highly stratified profiles. In this manner, by the end of this input stage, each slope unit is characterized by its own set of physical properties and FE mesh.

The processing stage is performed outside the GIS framework. First, each georeferenced grid is transformed into a column vector and arranged into j different subsets that share the same FE discretization parameters. For instance, in the schematic example shown in Fig. 1, three classes of slope thickness (and hence FE meshes) have been identified and labeled with different colors (i.e., $j = 1$ to 3). Since the FE algorithm has been written using an *array* programming structure (also referred to as *vectorized* form), operations apply simultaneously to all the slope units that are within a given subset j . This is highlighted in Fig. 1, for the subset $j = 3$, where the simulations for cells m_2 , m_6 , and m_7 are performed simultaneously. Note that even though they share the FE mesh and thickness, they might have different slope angles or hydro-mechanical properties, thus leading to different profiles of suction and/or FS. This computational sectorization becomes important depending on the spatial variability across the zone of study. For example, the study area of 9 km² shown in the next section contains more than $m = 3 \times 10^5$ cells (Fig. 2) with significant

differences in layering and thicknesses. Instead of running a sequence of m individual FE simulations to cover the entire landscape, a sequence of j vectorized simulations is performed, each applied over different cell clusters with the same thicknesses but spatially variable properties.

During the simulation of the infiltration process, the computed pore pressures are used to update the FS for each cell. If at any time step, the condition $FS < 1$ is fulfilled at any depth throughout the slope, then the corresponding time and depth of failure for that cell are stored in two different column vectors (i.e., t_f and z_f , respectively in Fig. 1). If the slope remains stable during the storm, then a non-data index is assigned to such output cells. The final stage consists on transforming the resulting t_f and z_f vectors into the original georeferenced grid and the generation of raster files. Lastly, postprocessing steps such as map visualization at different times are performed through a GIS platform.

Case study

Site datasets

The proposed approach is here used to analyze a series of documented shallow landslides that occurred in Campania (Southern Italy). Detailed analyses of the characteristics of the events have been reported elsewhere (Cascini et al. 2008; Crosta and Dal Negro 2003; Guadagno et al. 2005). Here only a brief description of the site-specific input datasets used for the simulations is presented.

The region of interest covers an area of approximately 9 km² and is located in the Pizzo d'Alvano massif, on the vicinity of the Sarno municipality (Fig. 2). A 4 × 4 m digital elevation model (DEM) was used to define the size of the slope units. Such size is lower than the smallest landslide (36 m²), thus providing an appropriate spatial resolution for mapping the results of the simulations.

On May 4–5 of 1998, after more than 48 h of rainfall, several shallow landslides were triggered across the massif (Frattini et al. 2004). Based on field surveys and post-event aerial photos, Crosta and Dal Negro (2003) mapped 47 landslide scars (red contours on Fig. 2). Cascini et al. (2011) reconstructed the temporal sequence for most of the failures by analyzing the reported arrival time of landslide masses. Their results are shown in Fig. 2 as dashed elliptical contours and labeled according to their estimated failure times. Other authors have reported landslide triggering during the last 10 h of the storm (Crosta and Dal Negro 2003). This value provides a lower bound estimate for the lack of reported failure times in the central sector (Fig. 2).

The site is located approximately 20 km east of the Somma-Vesuvius volcanic system. Due to such proximity, the slopes are mantled by air-fall pyroclastic deposits associated with different phases of volcanic activity (De Vita et al. 2006). As a result, alternations of ashes (with thickness between 40 to 60 cm) and pumices (10 to 30 cm) are often found, resulting in stratified profiles across the landscape (Cascini et al. 2014). The simplified soil profile derived from average thickness values proposed by Crosta and Dal Negro (2003) will be adopted here for the thicker slopes of 2 m (Fig. 3c). Furthermore, the hydrologic properties of the ashes vary according to their deposition history and depth (Sorbinio and Nicotera 2013). As a consequence, two types of ash, labeled here as A and B (for the upper and buried ashes, respectively), have been used.

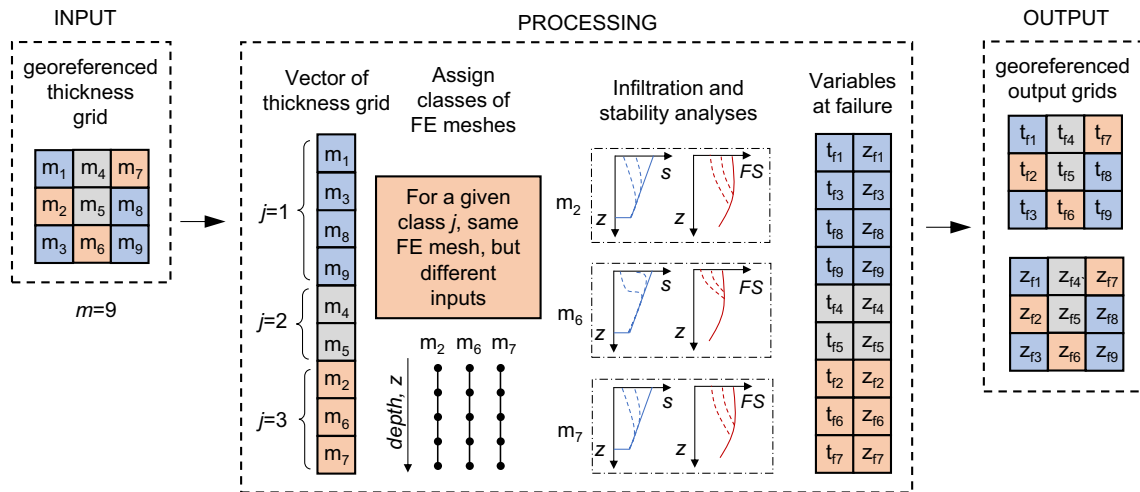


Fig. 1 Schematic representation of model workflow: m = number of cells, j = number of cell classes with the same FE mesh, t_f = time to failure, z_f = failure depth, s = suction, FS = factor of safety. To efficiently distribute the computational cost of the simulations, different FE meshes can be used for distinct sectors of the landscape

In addition to stratigraphic heterogeneity, the thickness of the covers varies spatially (De Vita et al. 2006). Particularly, higher elevations are characterized by smaller depths to bedrock (between 0.5 and 2 m), while lower zones present much thicker deposits (larger than 5 m). The distribution proposed by Cascini et al. (2008) was adopted in this study, and accordingly, different FE meshes were implemented for each class of thickness (Fig. 2). The corresponding stratified profiles (Fig. 3a, b) were chosen to keep the same layering sequence of the thicker slope and reflect an increase in vertical heterogeneity with burial depth, which is in agreement with field observations (Crosta

and Dal Negro 2003). Initial hydrostatic conditions with suction values of 20 kPa at the soil-bedrock interface were used on the basis of monthly averaged suction profiles measured on monitoring hillslopes of the area (Pirone et al. 2015), while zero-flux basal boundary conditions were assumed. Lastly, rainfall data measured from the closest meteorological station were used (Frattini et al. 2004).

The calibration of the hydrologic parameters for each of the layers is shown in Fig. 4. While the water retention properties were derived from pressure plate measurements (thus referring to the drying branch of the retention curve), evidence reported by Sorbino and

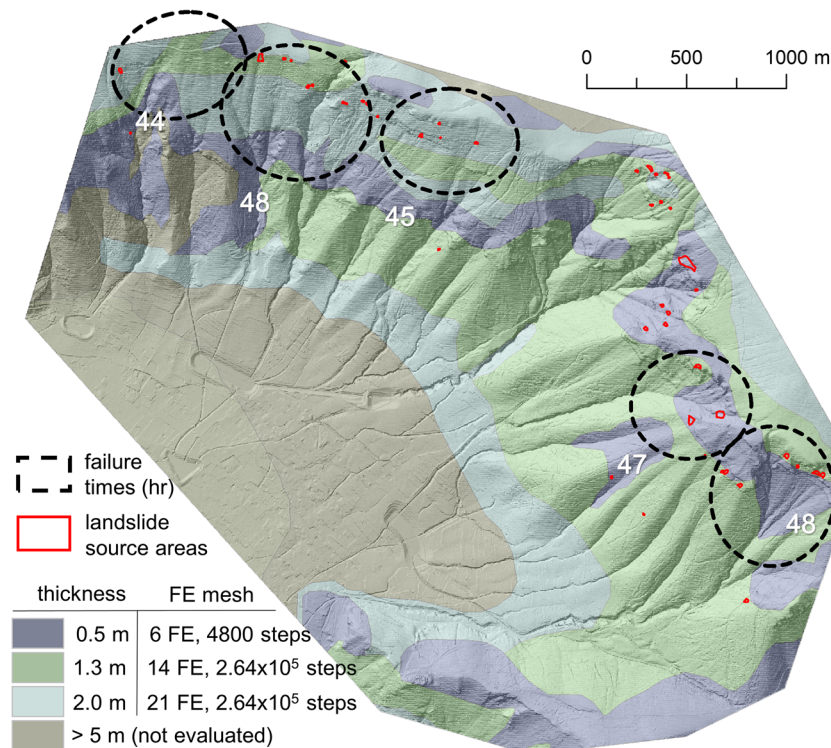


Fig. 2 Landslide inventory and input datasets: spatial distribution of thickness (Cascini et al. 2008), FE meshes, landslide source areas (Crosta and Dal Negro 2003), and reported contours of failure time (Cascini et al. 2011)

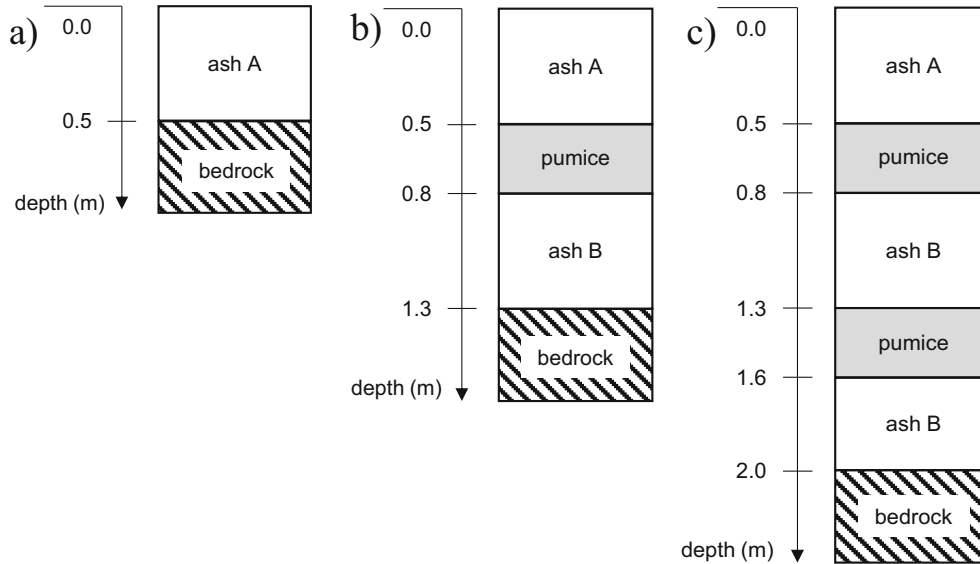


Fig. 3 Stratigraphic profiles adopted for the analysis of the three classes of thickness considered in this study; **a** 0.5 m, **b** 1.3 m, and **c** 2.0 m (based on Crosta and Dal Negro 2003)

Foresta (2002) for soils of the same area suggests that hysteretic effects are negligible at confinement pressures typical of shallow slopes, thus making the data reported in Fig. 4 a viable simplification for the following analyses. The Van Genuchten (VG) model is used for both water retention and the HCF. Note that the pumice presents a value of saturated hydraulic conductivity K_s three orders of magnitude higher than ash B. This causes a much faster propagation of the infiltration front through these layers, thus requiring a larger number of time steps to capture such abrupt process.

The strength parameters for ash B ($k = 0.6$, $\phi' = 38^\circ$) were calibrated from shear test data at different levels of confinement and suction and discussed in detail in (Lizárraga et al. 2017). Slight variations in friction angle are found between the ashes (Pirone et al. 2015), while consistent data for pumices is scarce. Hence, the same set of mechanical parameters have been used for each layer.

Model scenarios based on homogeneous slope profiles

To analyze the role of the stratigraphy, two additional scenarios based on homogeneous slope profiles have been considered. Since K_s presents a high layer-to-layer variability and exerts a key influence on the hydrologic response, its representative values have been defined on the basis of two distinct averaging procedures. The rest of the model parameters have instead been assumed identical to those of ash B due to its larger thickness (see Fig. 3). It is worth noting that the latter simplification plays a smaller role in the model predictions, due to the major effect played by K_s .

For groundwater flow, a weighted harmonic mean is often employed to define K_s (Zhu 2008):

$$K_s^{\text{harmonic}} = \frac{H}{\sum_{i=1}^{n_{\text{layers}}} \frac{h_{\text{layer}}}{K_s}} = \frac{2.0}{\frac{0.5}{K_{s \text{ ash A}}} + \frac{0.6}{K_{s \text{ pumice}}} + \frac{0.9}{K_{s \text{ ash B}}}} \approx 1 \times 10^{-6} \text{ ms}^{-1} \quad (3)$$

where n_{layers} is the number of layers, while H and h_{layer} indicate the total thickness of the slope and the thickness of individual layers, respectively. Since the harmonic mean is dominated by the

minimum of its arguments, it provides a lower bound of K_s (indeed the obtained value is closer to $K_{s \text{ ash A}}$). This value will be used for model scenario A. To test an upper bound value of K_s , a weighted arithmetic mean is also considered:

$$K_s^{\text{mean}} = \frac{1}{H} \sum_{i=1}^{n_{\text{layers}}} (h_{\text{layer}} K_s) = \frac{0.5 K_{s \text{ ash A}} + 0.6 K_{s \text{ pumice}} + 0.9 K_{s \text{ ash B}}}{2.0} \approx 3 \times 10^{-5} \text{ ms}^{-1} \quad (4)$$

which is closer to $K_{s \text{ pumice}}$. Such value falls within the range reported by (Cascini et al. 2011) and has been used to provide a first-order estimate of hydrologic response in stratified slopes. In the following, it will be used for model scenario B. The stratified model is hereafter referred to as model scenario S.

Analyses and results

Spatial performance

The computed susceptibility map using the homogeneous model A is first shown in Fig. 5. Each unstable cell is associated with different color levels that reflect the corresponding failure times, thus allowing a direct inspection of the spatial and temporal model response.

To allow a better visual inspection, three insets are shown at a higher spatial resolution and are located at the western, central, and eastern part of the landscape (insets A, B, and C, respectively). An acceptable spatial performance is observed on the eastern sector (inset C). However, the model vastly underperforms on the west and center part of the zone of study. For instance, consider insets A and B which contain 21 documented landslides (red contours), i.e. approximately 40% of the entire inventory. Not only there is a significant underestimation of unstable area, but also the few model predictions fall outside the reported landslide contours.

The simulation results for model B are shown in Fig. 6. Due to the higher homogenized value of K_s , the amount of computed unstable area increased by a factor of five across the landscape.

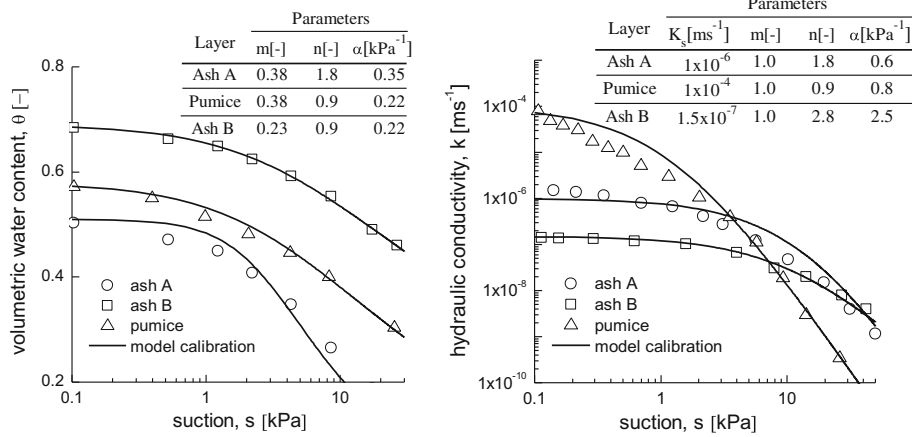


Fig. 4 Calibration of hydrologic parameters: a water retention curve (data after Crosta and Dal Negro 2003), b hydraulic conductivity function (data after Pirone et al. 2015). Parameter values corresponding to the Van Genuchten model

The improved performance within insets A and B came at the expense of an overall increase of overpredictions, as can be found in the central sector and in the westernmost part of the landscape, where clusters of predicted unstable cells not only fall outside landslide source areas, but also outside the elliptic dashed contours.

A closer inspection of the color scale suggests a prevalence of computed failure times at the early stages of the analysis. For instance, the majority of predictions within inset A failed around 30 h, which is much earlier than the reported estimates (between 45 and 48 h in that zone). A similar case occurs within inset C, where the computed failure times fall around 41 h, earlier than the reported estimates of 47–48 h (see next section for further analyses of temporal performance). Indeed, within this latter zone, the

previous model provided better results (compare with inset C of Fig. 5).

The computed susceptibility map using the stratified model is shown in Fig. 7. This scenario results in an intermediate level of unstable area that provides a good spatial model performance across the landscape. For instance, unlike model A, the computed unstable cells in the western and central sectors are in better agreement with landslide source areas, while at the same time, the level of overpredictions is reduced compared to model B. Indeed, the ratio of successful model computations versus overpredictions (i.e., false positives), often used as a spatial performance metric (Sorbinio et al. 2010), increased by 15%. More importantly, as it will be shown in the next section, the temporal performance over the whole area was not compromised. Indeed,

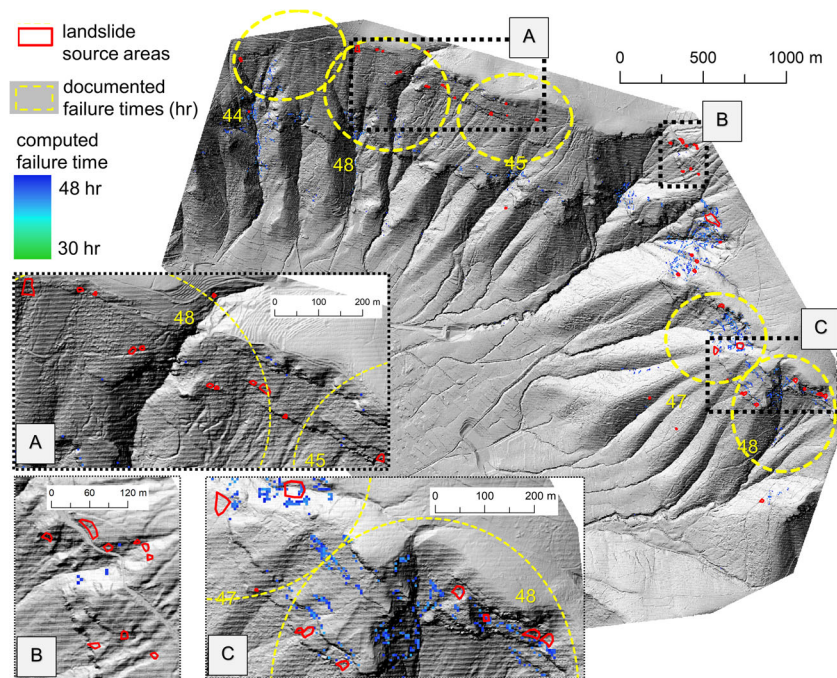


Fig. 5 Results of simulation for model scenario A (homogenized permeability; weighted harmonic mean)

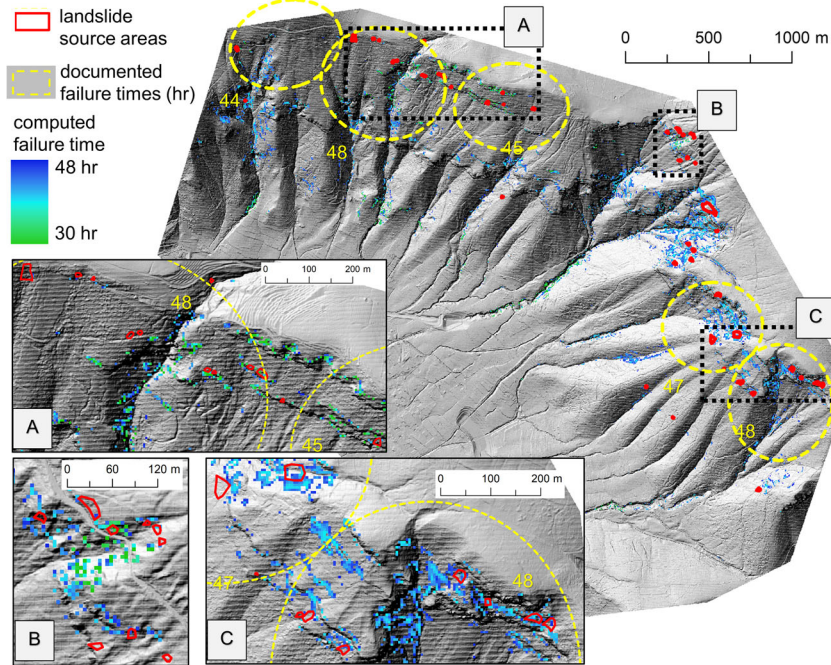


Fig. 6 Results of simulation for model scenario B (homogenized permeability, weighted arithmetic mean)

the computed unstable cells within insets A and C are accompanied by predicted failure times that are closer to the reported values.

In summary, the obtained results indicate that the use of homogeneous slopes based on harmonic mean values of K_s leads to poor spatial performances (model A), while the use of a constant K_s based on an arithmetic mean and layered profiles (models B

and S, respectively) improves such aspect. To complete the assessment of the model results, the next sections focus on the evaluation of temporal performance and predicted failure depths.

Temporal performance

The previous results suggest that the evaluation of physically based models should incorporate an analysis of their temporal response,

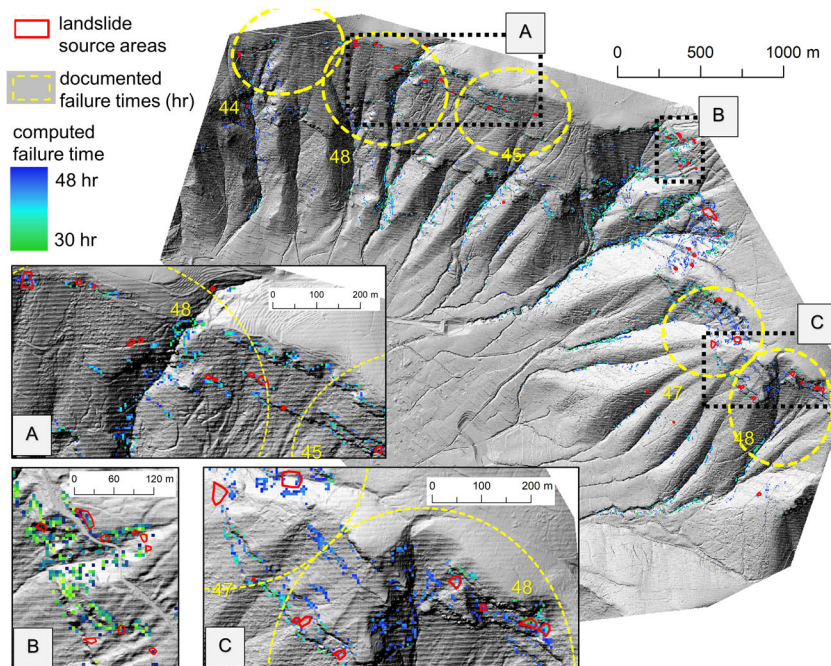


Fig. 7 Results of simulation for model scenario S (heterogeneous permeability; layered slopes)

since different model assumptions can lead to similar spatial clusters of unstable cells within certain sub-regions of the landscape (compare insets C of Figs. 5 and 7). To analyze this aspect, the statistical distributions of predicted unstable times (using bins of 2 h) within selected contours of failure time (those labeled by 44, 45, and 47 in Fig. 7) are shown in Fig. 8 for each of the previous simulations.

The results of the stratified model S are first shown in Fig. 8a–c. In general, the reported failure times are in close agreement with the peaks of the histograms, thus suggesting a good temporal performance. While it can be argued that Fig. 8b shows a wider variability in temporal predictions, it still produced better results than the other model scenarios (compare with Fig. 8e, h).

With regard to the simulations based on homogeneous profiles, model A performed better in the eastern part of the landscape (Fig. 8f), where all the predictions occurred within the interval of 44–48 h. However, it underperformed in the other sectors. In fact, the few predictions for Fig. 8d, e are associated with poor spatial performance (see Fig. 5). Alternatively, the simulations for model B (Fig. 8g–i) were characterized by dominant failure times that were computed earlier than the reported values. For instance, the

histogram in Fig. 8h shows that the most frequent failure time is 32 h, which is much earlier than the reported estimate of 45 h. These analyses corroborate the observations drawn from the susceptibility maps which suggested a prevalence of computed failure times at early stages (Fig. 6).

In most cases, contours of failure times are not reported, and only a general description of the triggering sequence is provided. For the selected case, landslides at the eastern and western parts of the landscape were reported to occur during the last 4 h of the storm (see Fig. 7). Although there are no reports for the central sector, a lower bound estimate can be 38 h (i.e., 10 h before the end of the storm), since several authors used this as the earliest estimate of failure time across the region. Within this context, a first-order evaluation of the model computations can be obtained by analyzing the sequence at which unstable cells start to appear over the landscape and comparing it against the reported data. To this aim, consider first Fig. 9, which shows the predicted unstable area for each model scenario during the last 24 h of the storm.

It is evident that by the end of the storm, model B computes the largest amount of unstable area. Note also that for model B, the

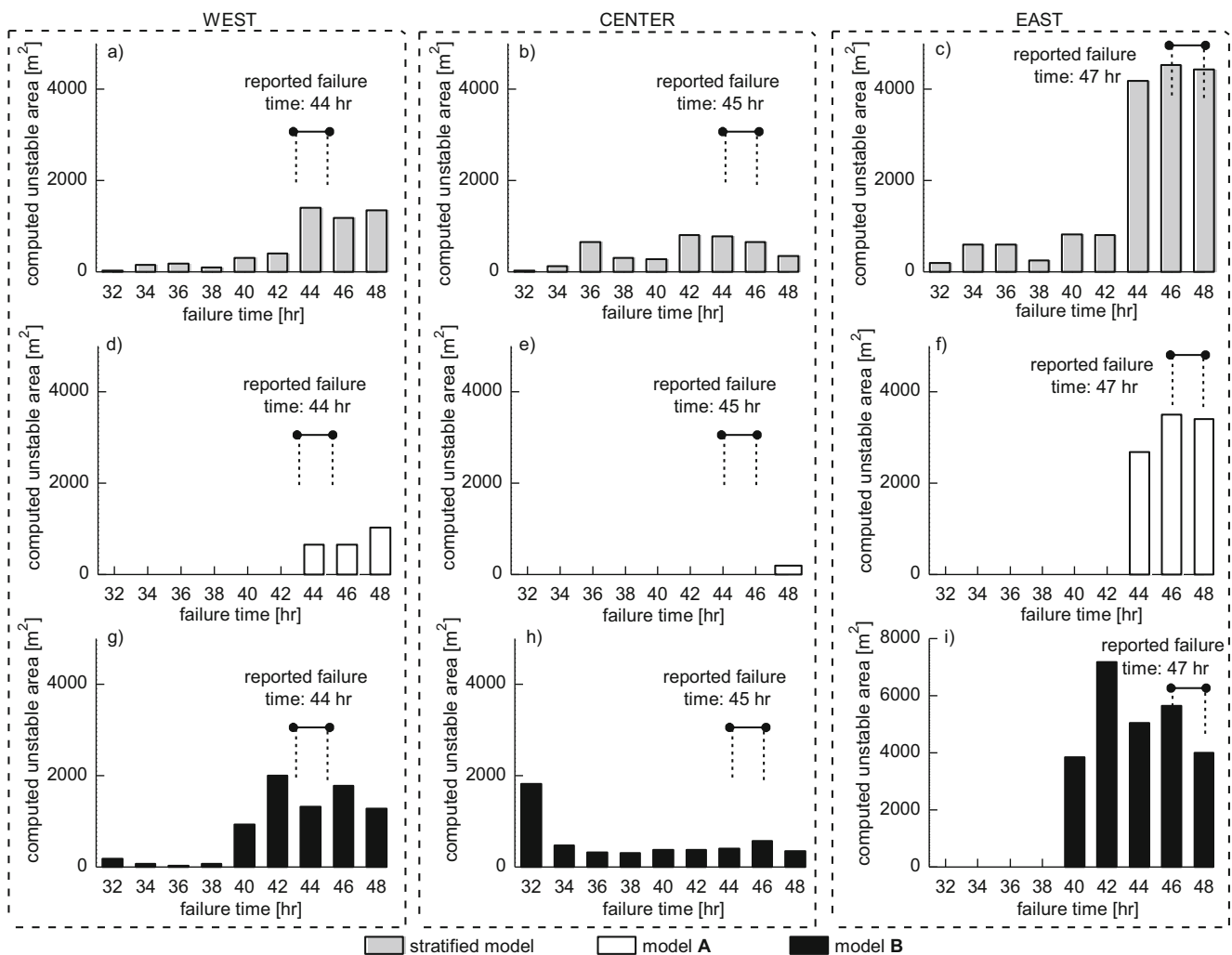


Fig. 8 Histograms of computed failure times within zones of reported slope instability. The west, center, and east sectors refer to the areas enclosed by the elliptical contours labeled as 44, 45, and 47, respectively (Fig. 7)

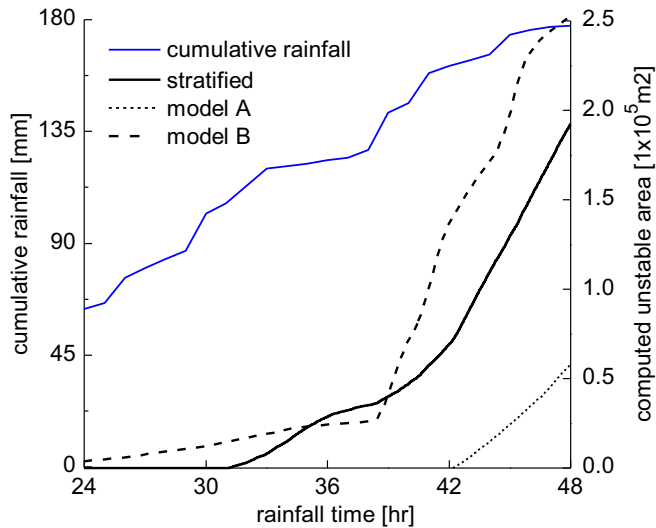


Fig. 9 Temporal evolution of the unstable area for the entire landscape

earliest predictions start at 24 h, while for model S, they occur at 32 h. What is not evident from this plot is that such early predictions are related to different spatial locations, thus implying a distinct computed sequence of landslide triggering.

To illustrate this aspect, Fig. 10a shows the temporal evolution of unstable area for the western, central, and eastern sectors of the landscape as predicted by the stratified model (the central sector refers to the region with no contours of failure time in Fig. 7). For times earlier than 40 h, the majority of predictions are associated with the central sector, while the eastern and western sectors failed almost simultaneously during the last 6 h of the simulation (similar to the reported data). Therefore, the computed triggering sequence starts at the center and then moves to the rest of the landscape. For the homogeneous model A (Fig. 10b), all the predictions occur during the last 6 h of the storm; however, as discussed, they are associated with poor spatial performance in the east and central sectors. Alternatively, for the homogeneous model B (Fig. 10c), failures are first computed in the western part (starting around 24 h), followed by the central and eastern sectors. While for the present case, there are no contours of failure times at the central zone, the western and eastern sectors have been reported to occur at times no earlier than 44 h, thus indicating that the homogeneous model B provides not only mismatches in failure times but also a different sequence of predictions. In summary, the previous analyses indicate that the sole evaluation of temporal evolution of unstable area over the entire landscape provides limited information about the model response, since similar temporal curves can be associated with different spatial locations. Furthermore, while it must be noted that factors not included in the current analyses may also contribute to the temporal sequence of landslide triggering (e.g., spatially varying rainfall, vegetation, local topographic features), these results demonstrate that variations in hydrologic properties across the slope profiles exert a major role on the temporal dynamics of failure and must not be neglected when an accurate interpretation of the sequence of events is necessary.

Failure depths

Stratigraphy not only affects the spatial and temporal model computations, but also the vertical location at which instability occurs,

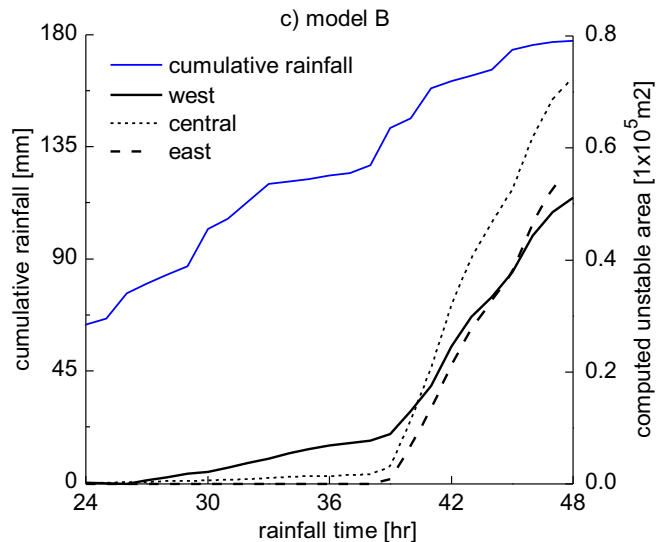
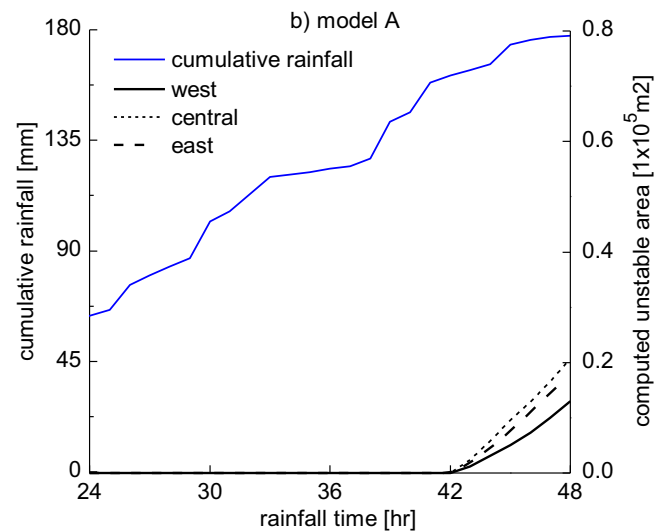
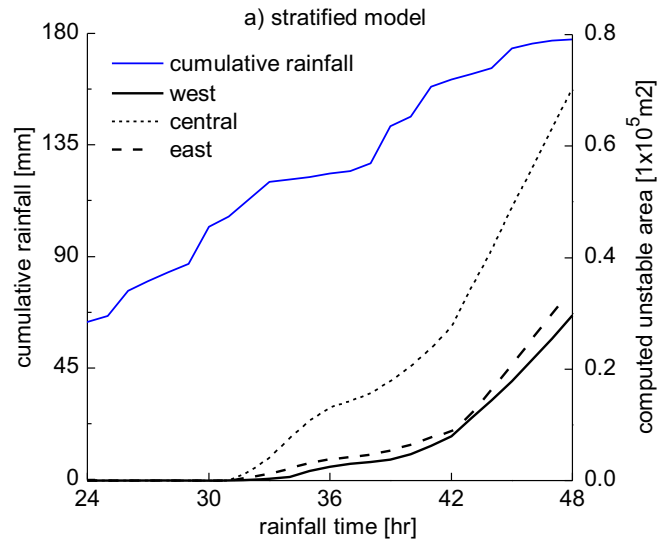


Fig. 10 Temporal evolution of the unstable area for different sectors of the landscape: a stratified model S; b homogeneous model A; homogeneous model B

thus providing additional information that can be used to evaluate the model computations. For this purpose, consider Fig. 11 a, which shows the histogram of computed failure depths for the stratified model. The results indicate that, except few deep failures occurred at 2 m, most of the unstable zones were located at the interfaces between ashes and pumices. Indeed, the most frequent failure depth was located at 0.80 m (i.e., at the upper pumice/ash B interface).

Alternatively, for the homogeneous model A (Fig. 11b), all the unstable cells were computed to occur at 0.50 m and all of them were located at slopes with thickness of equal depth (the thicker slopes remained stable). For model B (Fig. 11c), failures were computed in thicker slopes; however, all the unstable depths were located at the base (at 0.50 m, 1.30 m, and 2.0 m). In other words, for homogeneous slopes, the distribution of failure depths is dependent on the adopted thickness, while for stratified covers, failure can be expected either at the base of the slopes or at layer interfaces. Lastly, Fig. 11d shows the statistical distribution of failure depths from 26 landslide source areas (Crosta and Dal Negro 2003). While such sample is of limited size, it displays a wide variability of failure depths that is highly influenced by complex sequences of layering, thus highlighting the importance of such effects.

Discussion

The analyses indicated how stratigraphy influences the spatial and temporal patterns of landslide triggering. To provide a physical interpretation of such variability, it is useful to analyze the hydrologic response of a single slope within the landscape. This is first shown for the homogenous model A (Fig. 12a) in terms of computed profiles of pore water pressure p_w . By the end of the storm,

the most critical section in the slope is located at the base, where moisture has been accumulated and a value of $p_w = -10$ kPa was computed, which is not enough to mobilize failure. Alternatively, for the homogeneous model B (Fig. 12b) characterized by a higher value of K_s , the infiltration front propagates much faster, so that the previous basal value of $p_w = -10$ kPa is reached at approximately 24 h. Evidently, this is the result of the augmented value of K_s induced by the selected homogenization procedure. Lastly, the results for the stratified model are shown in Fig. 12c. Note that transient spikes of pore pressure develop at the different ash/pumice interfaces. Such behavior is promoted by the large contrasts of K_s , in which the underlying ash acts as a temporarily impermeable barrier (Mancarella et al. 2012). If failure does not occur during this pore pressure transient, the ash saturates and starts to slowly allow drainage, thus enabling the propagation of the infiltration front to deeper layers that are sustaining higher overburden stresses.

These results are in agreement with reported triggering thresholds derived from 2D numerical analyses performed at hillslope scale (De Vita et al. 2013), thus confirming the key role of capillary barriers on landslide susceptibility, especially in stratified settings.

The previous considerations highlight the challenges of using homogenized profiles for layered slopes. If the properties of a single-layer are used to define the parameters of the entire slope, then the question becomes, which layer should be chosen as the most representative. If homogenization or averaging techniques are used, then the computed pore pressure profiles cannot be directly compared against field monitoring data, since the homogenized value of K_s is not a measurable quantity, but rather a numerical parameter introduced to adjust the timescale of the

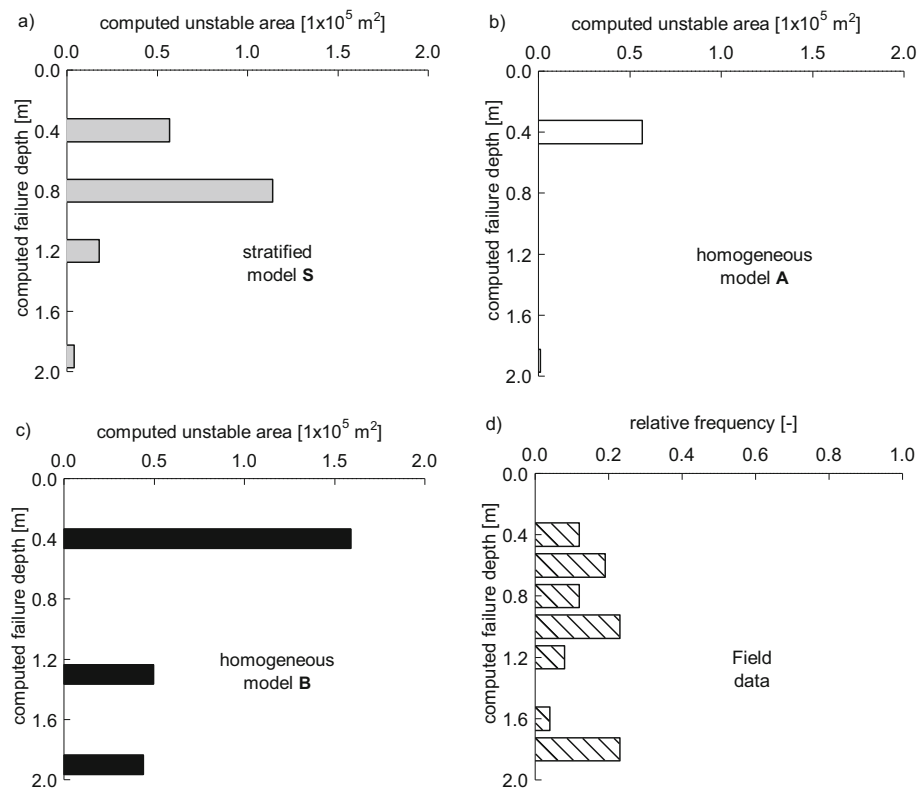


Fig. 11 Distribution of computed failure depths: a stratified model S, b homogeneous model A, c homogeneous model B, d field data (after Crosta and Dal Negro 2003)

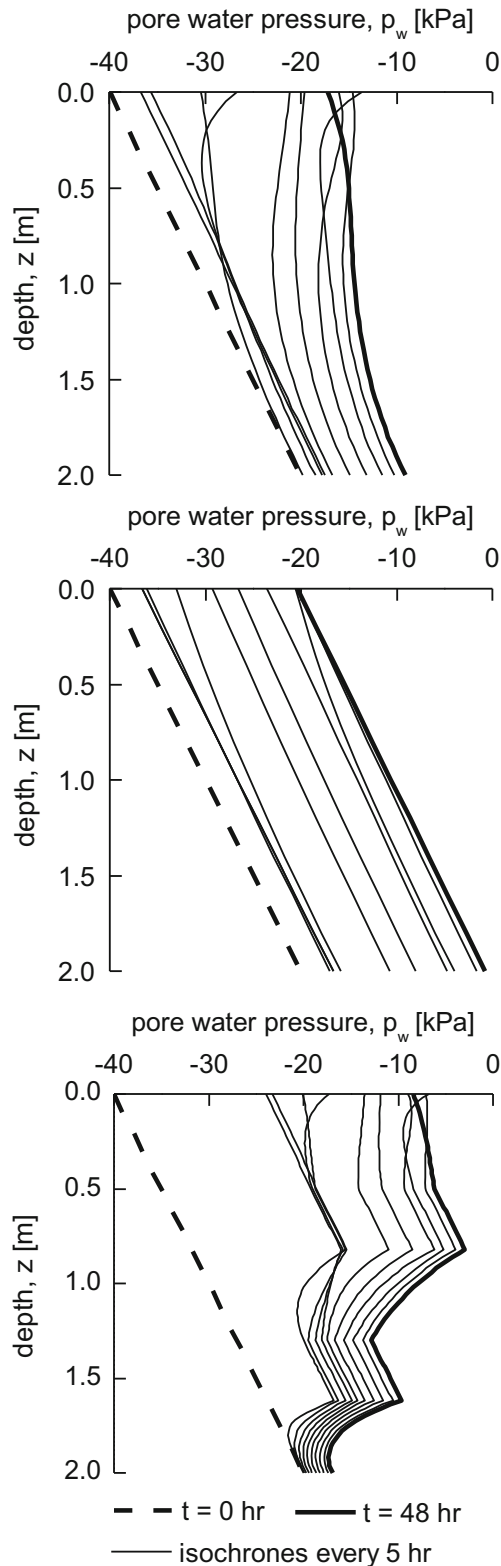


Fig. 12 Computed profiles of pore pressure: a homogeneous model A; b homogeneous model B; c stratified model S

problem. Besides, in principle, multiple hydrologic and mechanical parameters should be averaged, since K_s is not the only variable changing from one layer to another. Such considerations pose

even more uncertainty when landslide forecasting is required, in that homogenization techniques cannot accommodate spatially varying strength or failure mechanisms, which by their own nature may be highly localized and therefore very much dependent on the frictional properties of the layers which are eventually mobilized.

In light of the above results, it is evident that physically based models should provide not only information about whether a slope will fail or not (i.e., spatial performance), but they should also provide a consistent distribution of failure times and depths. Only in this manner, detailed field observations and experimental datasets can be used to constrain input data and/or evaluate the model performance.

Conclusions

A physically based model for the efficient generation of dynamic landslide susceptibility mapping in stratified settings has been presented. The proposed framework enables the incorporation of georeferenced datasets to define the spatial distribution of material properties, rainfall intensities, and initial and boundary conditions. Moreover, it relies on a vectorized solver that allows multiple simulations of transient infiltration in unsaturated slopes that share the same numerical discretization parameters (i.e., mesh and time steps).

The model was used to analyze a series of documented shallow landslides that occurred in a mountainous landscape covered by stratified volcanic soils. Laboratory and field data have been used to constrain the input parameters. In addition to the stratified model, two further scenarios based on homogeneous profiles and different values of hydraulic conductivity were considered. The results indicate that the use of layered profiles leads not only to a satisfactory spatial performance, but also to computed failure times and depths that are consistent with the landslide inventory. Alternatively, the use of homogeneous profiles based on averaged values of K_s provides a spatial performance which is acceptable only in selected portions of the landscape, as well as to poor predictions of failure time and inaccurate computations of failure depth (always located at the base of the slopes).

The proposed physically based model fosters the use of laboratory data and field measurements to constrain input data, as well as the assessment of model predictions in light of metrics which are often ignored in the context of spatially distributed landslide forecasting. For instance, complex stratigraphy, advanced hydrologic models, and varying initial and boundary conditions can all be incorporated in the proposed approach. Furthermore, information from landslide inventories such as distribution of failure depth and spatiotemporal sequences of landslide triggering can be used to back-analyze case studies. In other words, the simulation platform presented in this paper aims to provide an efficient tool to optimize the use of available data and reduce the uncertainty of model computations in hazard management studies.

Funding information This work was supported by Grant No. CMMI-1324834 awarded by the US National Science Foundation.

References

- Baum RL, Coe JA, Godt JW, Harp EL, Reid ME, Savage WZ, Schulz WH, Brien DL, Chleborad AF, McKenna JP (2005) Regional landslide-hazard assessment for Seattle, Washington, USA. *Landslides* 2(4):266–279
- Baum RL, Godt JW, and Savage WZ, (2010) Estimating the timing and location of shallow rainfall-induced landslides using a model for transient, unsaturated infiltration. *Journal of Geophysical Research: Earth Surface*, v. 115, no. F3

- Bilotta E, Cascini L, Foresta V, Sorbinow G (2005) Geotechnical characterisation of pyroclastic soils involved in huge flowslides. *Geotech Geol Eng* 23(4):365–402
- Camporese M, Paniconi C, Putti M, Orlandini S (2010) Surface-subsurface flow modeling with path-based runoff routing, boundary condition-based coupling, and assimilation of multisource observation data. *Water Resour Res* 46(2)
- Cascini L, Cuomo S, and Della Sala M (2011) Spatial and temporal occurrence of rainfall-induced shallow landslides of flow type: a case of Sarno-Quindici, Italy: *Geomorphology*, 126(1):148–158
- Cascini L, Cuomo S, Guida D (2008) Typical source areas of May 1998 flow-like mass movements in the Campania region. Southern Italy: *Engineering Geology* 96(3):107–125
- Cascini L, Sorbino G, Cuomo S, Ferlisi S (2014) Seasonal effects of rainfall on the shallow pyroclastic deposits of the Campania region (southern Italy). *Landslides* 11(5):779–792
- Celia MA, Bouloutas ET, Zarba RL (1990) A general mass-conservative numerical solution for the unsaturated flow equation. *Water Resour Res* 26(7):1483–1496
- Chen HX, Zhang LM (2014) A physically-based distributed cell model for predicting regional rainfall-induced shallow slope failures. *Eng Geol* 176:79–92
- Chen Z, Huan G, and Ma Y (2006) Computational methods for multiphase flows in porous media, Siam
- Crosta G, Dal Negro P (2003) Observations and modelling of soil slip-debris flow initiation processes in pyroclastic deposits: the Sarno 1998 event. *Nat Hazards Earth Syst Sci* 3(1/2):53–69
- Crozier M (2005) Multiple-occurrence regional landslide events in New Zealand: hazard management issues. *Landslides* 2(4):247–256
- De Vita P, Agrello D, Ambrosino F (2006) Landslide susceptibility assessment in ash-fall pyroclastic deposits surrounding Mount Somma-Vesuvius: application of geophysical surveys for soil thickness mapping. *J Appl Geophys* 59(2):126–139
- De Vita P, Napolitano E, Godt JW, Baum RL (2013) Deterministic estimation of hydrological thresholds for shallow landslide initiation and slope stability models: case study from the Somma-Vesuvius area of southern Italy. *Landslides* 10(6):713–728
- Duncan JM, Wright SG, Brandon TL (2014) Soil strength and slope stability. John Wiley & Sons
- Frattini P, Crosta GB, Fusi N, Dal Negro P (2004) Shallow landslides in pyroclastic soils: a distributed modelling approach for hazard assessment. *Eng Geol* 73(3):277–295
- Fredlund D, Morgenstern NR, Widger R (1978) The shear strength of unsaturated soils. *Can Geotech J* 15(3):313–321
- Fressard M, Thiery Y, Maquaire O (2014) Which data for quantitative landslide susceptibility mapping at operational scale? Case study of the Pays d'Auge plateau hillslopes (Normandy, France). *Nat Hazards Earth Syst Sci* 14:569–588
- Godt J, Baum R, Savage W, Salciarini D, Schulz W, Harp E (2008) Transient deterministic shallow landslide modeling: requirements for susceptibility and hazard assessments in a GIS framework. *Eng Geol* 102(3):214–226
- Guadagno F, Forte R, Revellino P, Fiorillo F, and Focareta M (2005) Some aspects of the initiation of debris avalanches in the Campania Region: the role of morphological slope discontinuities and the development of failure: *Geomorphology*, v. 66(1):237–254
- Iverson RM (2000) Landslide triggering by rain infiltration. *Water Resour Res* 36(7):1897–1910
- Lizárraga JJ, Frattini P, Crosta GB, Buscarnera G (2017) Regional-scale modelling of shallow landslides with different initiation mechanisms: sliding versus liquefaction. *Eng Geol* 228:346–356
- Lu N, Godt J (2008) Infinite slope stability under steady unsaturated seepage conditions. *Water Resour Res* 44(11)
- Mancarella D, Doglioni A, Simeone V (2012) On capillary barrier effects and debris slide triggering in unsaturated layered covers. *Eng Geol* 147:14–27
- Montgomery DR, Dietrich WE (1994) A physically based model for the topographic control on shallow landsliding. *Water Resour Res* 30(4):1153–1171
- Pirone M, Papa R, Nicotera MV, Urciuoli G (2015) In situ monitoring of the groundwater field in an unsaturated pyroclastic slope for slope stability evaluation. *Landslides* 12(2):259–276
- Richards LA (1931) Capillary conduction of liquids through porous mediums. *Physics* 1(5):318–333
- Sorbino G, & Foresta, V. (2002). Unsaturated hydraulic characteristics of pyroclastic soils. In *Proceedings of the 3rd international conference on unsaturated soils* (Vol. 1, pp. 405–410). Rotterdam, the Netherlands: Balkema
- Sorbino G, Nicotera MV (2013) Unsaturated soil mechanics in rainfall-induced flow landslides. *Eng Geol* 165:105–132
- Sorbino G, Sica C, Cascini L (2010) Susceptibility analysis of shallow landslides source areas using physically based models. *Nat Hazards* 53(2):313–332
- Van Dam JC, Feddes RA (2000) Numerical simulation of infiltration, evaporation and shallow groundwater levels with the Richards equation. *J Hydrol* 233(1–4):72–85
- Van Westen C, Van Asch TW, Soeters R (2006) Landslide hazard and risk zonation—why is it still so difficult? *Bull Eng Geol Environ* 65(2):167–184
- Van Westen CJ, Castellanos E, Kuriakose SL (2008) Spatial data for landslide susceptibility, hazard, and vulnerability assessment: an overview. *Eng Geol* 102(3–4):112–131
- Zhu J (2008) Equivalent parallel and perpendicular unsaturated hydraulic conductivities: arithmetic mean or harmonic mean? *Soil Sci Soc Am J* 72(5):1226–1233
- Zienkiewicz, O. C., Chan, A., Pastor, M., Schrefler, B., and Shiomi, T., 1999, *Computational geomechanics*, Citeseer

J. J. Lizárraga · G. Buscarnera (✉)

Department of Civil and Environmental Engineering,
Northwestern University,
Evanston, IL, USA
Email: g-buscarnera@northwestern.edu